Scripta Materialia 209 (2022) 114384

Contents lists available at ScienceDirect

Scripta Materialia

journal homepage: www.elsevier.com/locate/scriptamat

Anisotropic grain boundary area and energy distributions in tungsten

Ooraphan Chirayutthanasak[a], Rajchawit Sarochawikasit[b], Apiwat Wisitsorasak[c,d], Nopporn Rujisamphan[a,d], Timofey Frolov[e], Tomas Oppelstrup[e], Somsak Dangtip[f], Gregory S. Rohrer[g,1], Sutatch Ratanaphan[a,d,h,*]

[a] Nanoscience and Nanotechnology Graduate Program, Faculty of Science, King Mongkut's University of Technology Thonburi, Bangkok 10140, Thailand
[b] Department of Computer Engineering, Faculty of Engineering, King Mongkut's University of Technology Thonburi, Bangkok 10140, Thailand
[c] Department of Physics, Faculty of Science, King Mongkut's University of Technology Thonburi, Bangkok 10140, Thailand
[d] Center of Excellence in Theoretical and Computational Science Center (TaCS-CoE), Faculty of Science, King Mongkut's University of Technology Thonburi, 126 Pracha Uthit Rd, Thung Khru, Bangkok 10140, Thailand
[e] Lawrence Livermore National Laboratory, Livermore, CA 94550-9234, United States of America
[f] Thailand Institute of Nuclear Technology, 9/9 Moo 7, Saimoon, Ongkharak, Nakhon Nayok 26120, Thailand
[g] Department of Materials Science and Engineering, Carnegie Mellon University, Pittsburgh, PA 15213-3890, USA
[h] Department of Tool and Materials Engineering, Faculty of Engineering, King Mongkut's University of Technology Thonburi, Bangkok 10140, Thailand

ARTICLE INFO

Article history:
Received 17 May 2021
Revised 25 September 2021
Accepted 27 October 2021

Keywords:
Modeling
Grain boundary energy
Grain boundary area
Tungsten

ABSTRACT

Describing microstructure evolution in tungsten requires a quantitative description of the anisotropic grain boundary energy. We present a grain boundary energy function for tungsten that specifies the energy of an arbitrary boundary given its five macroscopic crystallographic parameters. A comparison of measured grain boundary areas and the grain boundary energies given by the function at the Σ11, Σ17b, and Σ33a misorientations, which are problematic to determine by measurement or atomistic calculations, reveals inverse correlations that are similar to what have been observed in other metals.

Reducing the size of crystal grains to the nanoscale has been realized as a key principle for enhancing mechanical properties such as strength, hardness, and elongation of polycrystalline materials [1,2]. The relative areas of grain boundaries, known as grain boundary character distributions (GBCDs), are often correlated with the macroscopic behaviors of materials [2,3]. Grain boundary engineering (GBE) has been applied to various materials [2,3] for controlling the GBCDs. Considering that tungsten not only has the highest melting point of all elemental metals and a low-sputter erosion rate, and that its radiation resistance is also far greater than carbon fiber composite, beryllium, and iron, [4,5], tungsten has been chosen to be a key structural material for fusion energy systems. Because dislocation-grain boundary interactions and helium segregation depend on the structure of grain boundaries [6,7], tungsten with desired mechanical strength and irradiation resistance might be achieved by the GBE of the GBCDs.

While anisotropic GBCDs in face-centered cubic (FCC) metals strongly correlate with their grain boundary energy distributions (GBEDs) [8,9], the GBCDs in body-centered cubic (BCC) metals, such as tungsten, [10,11] are not clearly related to their GBEDs emphasizing the challenge in the applicability of GBE to BCC metals. While the energies of the Σ3 coherent twin boundary on {111} planes in FCC metals (Fe= 0.02 J/m^2, Cu= 0.04 J/m^2, and Ni= 0.13 J/m^2) [8,12] and the Σ3 coherent twin boundary on {211} planes in BCC metals (Fe= 0.26 J/m^2, Mo= 0.39 J/m^2, and W = 0.58 J/m^2) [13,14] have the lowest boundary energy for each metal, it should be noted that the anisotropies of grain boundary energies in the FCC and BCC metals are considerably different. Specifically, the energy ratios between the Σ3 coherent twin boundary and the average grain boundary energy in the FCC metals (Fe = 0.02, Cu = 0.03, Al= 0.14, and Ni = 0.06) are significantly lower than those in the BCC metals (Fe = 0.24, Mo = 0.25, and W = 0.25), leading to much larger populations, measured in units of multiples of a random distribution (MRD), of coherent twin boundaries in FCC metals (Fe = 502 MRD, Cu = 1200 MRD, Al = 28, 700 MRD, and Ni = 1100 MRD) than in BCC metals

* Corresponding author at: Department of Tool and Materials Engineering, Faculty of Engineering, King Mongkut's University of Technology Thonburi, Bangkok 10140, Thailand.
E-mail address: sutatch.ratanaphan@mail.kmutt.ac.th (S. Ratanaphan).

[1] Gregory S. Rohrer was an Editor of the journal during the review period of the article. To avoid a conflict of interest, Gregory S. Rohrer was blinded to the record and another editor processed this manuscript.

https://doi.org/10.1016/j.scriptamat.2021.114384
1359-6462/

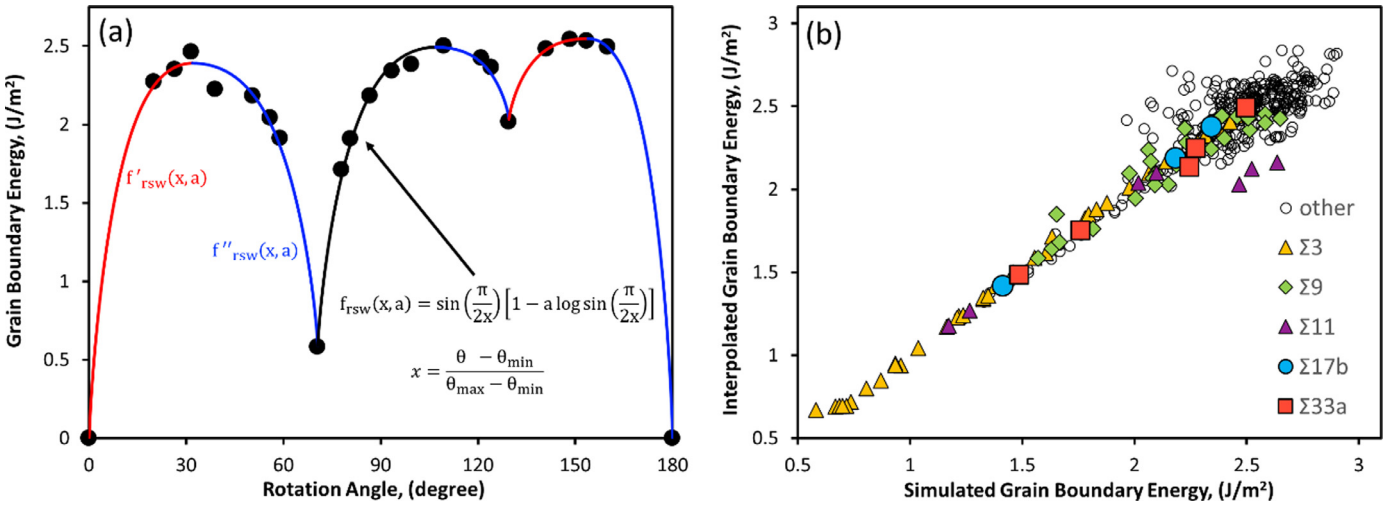

Fig. 1. The energies of [110] symmetric tilt boundaries fitted with the RSW functions [22,23] (a). Comparison between the simulated and interpolated grain boundary energies derived from our grain boundary function (b). These 408 boundaries can be categorized into six groups: Σ3 (yellow triangle), Σ9 (green diamond), Σ11 (purple triangle), Σ17b (blue circle), Σ33a (red square), and other (circle). (For interpretation of the references to color in this figure legend, the reader is referred to the web version of this article.).

(Fe = 13, 40 MRD, Mo = 2.3 MRD, and W = 2.9 MRD) [8–10,14–18]. In comparison to the FCC metals in which large fractions of the coherent twin boundary enhance the occurrences of twin-related domains (i.e. Σ3, Σ9, and Σ27) [19], it is necessary to consider the other low-energy grain boundaries for GBE of BCC metals.

Although we previously calculated 408 grain boundaries having 80 different misorientations using atomistic simulations [14], these grain boundary energies are only sufficient to describe the inverse relationship between grain boundary energy and population for the twin-related boundaries (i.e. Σ3, Σ9, and Σ27) in tungsten [14,20]. To fully investigate the network of low-energy grain boundaries, more extensive grain boundary energy data sets are required. By using interpolation between simulated grain boundary energies specified in the lower dimensions of the five macroscopic degrees of freedom (three for misorientation and two for plane inclination) [21], we successfully reconstructed the grain boundary energy function for BCC iron [11]. While the average grain boundary energy in W (2.32 J/m^2) is considerably larger than in Fe (1.12 J/m^2), the grain boundary energies in Fe and W are strongly correlated, similar to what has been reported for Fe and Mo [13,14]. Therefore, it is expected that the interpolation scheme for BCC Fe could be used to construct the grain boundary energy function for W. Comparisons between a larger grain boundary energy data set derived from our energy function and the anisotropic distributions of grain boundary area in tungsten [20] could enhance our understanding of the processing-microstructure-property relationships in GBE of BCC metals.

The grain boundary energy anisotropy was estimated from the energies of the 408 boundaries [14] using a scheme identical to the previous studies [11,21]. The Read–Shockley–Wolf (RSW) function [22], $f_{rsw}(x,\ a) = \sin(\frac{\pi}{2x})[1 - a\log\sin(\frac{\pi}{2x})], x = \frac{\theta - \theta_{min}}{\theta_{max} - \theta_{min}}$, is primarily used to interpolate the energy of a given boundary between the proximal boundaries with known energies. θ is the misorientation angle and a is a shape parameter [11]. Three subsets of high-symmetry grain boundaries with ⟨100⟩, ⟨110⟩, and ⟨111⟩ rotation axes are selected as the lower dimensions for the interpolation function, described in detail in the supplementary data and also in our recent study [11]. For example, Fig. 1**a** shows the energies of the symmetric tilt boundaries on the [110] axis that are well described by the RSW function [22,23]. Fig. 1**b** shows the relationship between the simulated energies of 408 grain boundaries and the energies of the same boundaries derived from the grain boundary energy function. Although there is some scatter for the high-energy boundaries, the interpolated and simulated energies are strongly correlated with a correlation coefficient of 0.95 and a root mean square error of 0.14 J/m^2, suggesting that the energies of arbitrary grain boundaries can also be successfully determined from the energy function. Large data sets of interpolated grain boundary energies (i.e. Σ3, Σ7, Σ11, Σ15, Σ17a, Σ17b, and Σ33a) are then compared with the grain boundary population in nanocrystalline tungsten measured by transmission electron microscopy [20].

Fig. 2 compares the grain boundary population in tungsten [20] and the energies interpolated using our energy function. Grain boundaries with specific misorientations (Σ33a, 20.05°/ [110], Σ11, 50.48°/ [110], and Σ17b, 61.93°/ [212]) are selected as nominal examples within the entire range of the disorientation angle distribution in tungsten [20] as shown in Fig. 2**a**. For these misorientations, the grain boundary populations inversely correlate with the interpolated energies. Interestingly, the peak positions for the Σ33a (Fig. 2**b**), Σ11 (Fig. 2**c**), and Σ17b (Fig. 2**d**) are centered around the {110} symmetric twist boundaries corresponding to the lowest grain boundary energy at each misorientation (Σ11 (1.27 J/m^2), Σ17b (1.42 J/m^2), and Σ33a (1.49 J/m^2)). The low energies of these symmetric twist boundaries likely arise from the {110} bounding planes, which have the lowest surface energy [13].

Fig. 3 shows point-by-point comparisons between the measured grain boundary populations and interpolated energies. Interestingly, the inverse relationships are only observed for the grain boundaries in which energy anisotropies, calculated from the energy differences between the maximum and minimum energies at a specific misorientation, are greater than 1 J/m^2 (see Fig. 3**a** and Table 1). Those boundaries with smaller anisotropies also have higher average energies. Because of this, they occur more infrequently, and it is difficult to accurately measure their relative areas. Therefore, the absence of the inverse correlation of population and energy for low energy anisotropy boundaries might be associated with limitations of the measurement [25]. As examples of high-energy anisotropy boundaries, relationships between grain boundary populations and energies for the Σ3 (1.83 J/m^2), Σ11 (1.01 J/m^2), Σ17b (1.31 J/m^2), and Σ33a (1.01 J/m^2) misorientations are shown in Fig. 3**b**. Because the maximum energies in Fig. 3**a** are rather similar, the energy anisotropies mainly depend on the

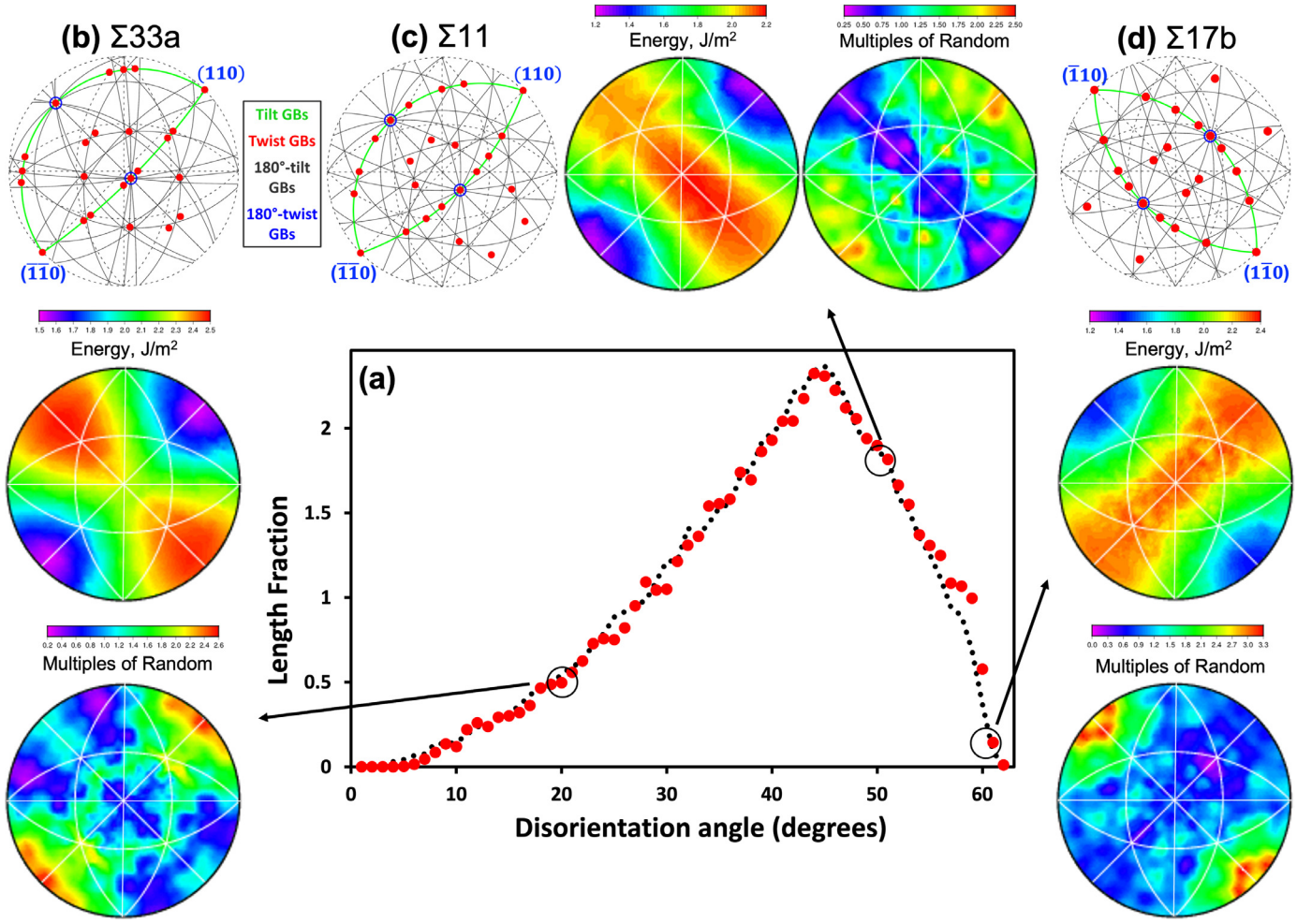

Fig. 2. Disorientation angle distribution of tungsten (large red circles) [20] is consistent with a random distribution (small black circles) (a). The interpolated grain boundary energies inversely correlate with the measured grain boundary areas for Σ33a (b), Σ11 (c) and 17b (d) misorientations [10]. The relative grain boundary areas are plotted in units of multiples of a random distribution (MRD). Schematic representations of grain boundaries at Σ33a, 20.1°/ [110], Σ11, 50.48°/ [110], and Σ17b, 61.93°/ [212] are produced from GBToolbox [24]. (For interpretation of the references to color in this figure legend, the reader is referred to the web version of this article.).

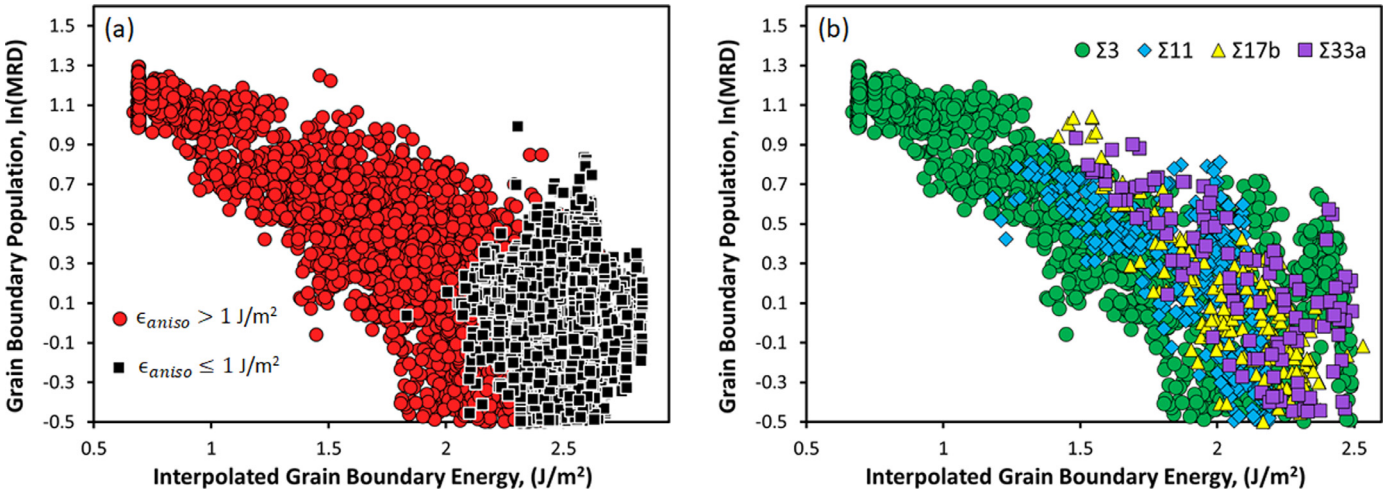

Fig. 3. Relationships between the interpolated grain boundary energies and grain boundary areas in tungsten [20]. Note that the data are classified into two groups based on the energy anisotropies in Table 1: low ($\epsilon_{aniso} \leq 1$ J/m^2) and high ($\epsilon_{aniso} > 1$ J/m^2) anisotropies marked by black squares and red circles, respectively (a). High-energy anisotropies with Σ3, Σ11, Σ17b, and Σ33a misorientations are marked with green circles, blue diamonds, yellow triangles, and purple squares, respectively (b) (For interpretation of the references to color in this figure legend, the reader is referred to the web version of this article.).

Table 1
Maximum (ϵ_{max}), minimum energy (ϵ_{min}), energy anisotropy (ϵ_{aniso}), and correlation coefficient at fixed Σ.

Σ	Number of GBs	ϵ_{max}, J/m^2	ϵ_{min}, J/m^2	ϵ_{aniso}, J/m^2	Correlation Coefficient
3	1426	2.505	0.671	1.834	−0.87
5	940	2.320	2.007	0.313	−0.58
7	616	2.642	2.412	0.230	0.38
9	995	2.477	1.460	1.017	−0.80
11	436	2.193	1.179	1.014	−0.70
13a	186	2.839	2.066	0.773	0.12
13b	219	2.583	2.469	0.114	0.35
15	878	2.689	2.527	0.162	0.10
17a	112	2.773	2.157	0.615	−0.27
17b	202	2.727	1.418	1.308	−0.80
19a	171	2.547	1.513	1.034	−0.76
19b	110	2.621	2.084	0.537	0.57
21a	169	2.453	2.348	0.106	0.12
21b	486	2.566	2.421	0.145	0.16
23	223	2.589	2.489	0.099	−0.09
25a	125	2.741	1.833	0.908	0.16
25b	417	2.524	2.235	0.289	−0.35
27a	204	2.537	1.502	1.035	−0.74
27b	362	2.679	2.492	0.186	0.05
29a	31	2.647	2.334	0.314	−0.64
29b	129	2.642	2.395	0.247	−0.35
31a	33	2.307	2.195	0.112	0.33
31b	104	2.535	2.311	0.223	−0.25
33a	131	2.493	1.485	1.009	−0.74
33b	173	2.667	1.659	1.008	−0.26
33c	127	2.396	1.376	1.020	−0.78
35a	260	2.573	2.456	0.116	−0.02
35b	222	2.580	2.359	0.221	−0.37
All	39,554	2.840	0.666	2.174	−0.53

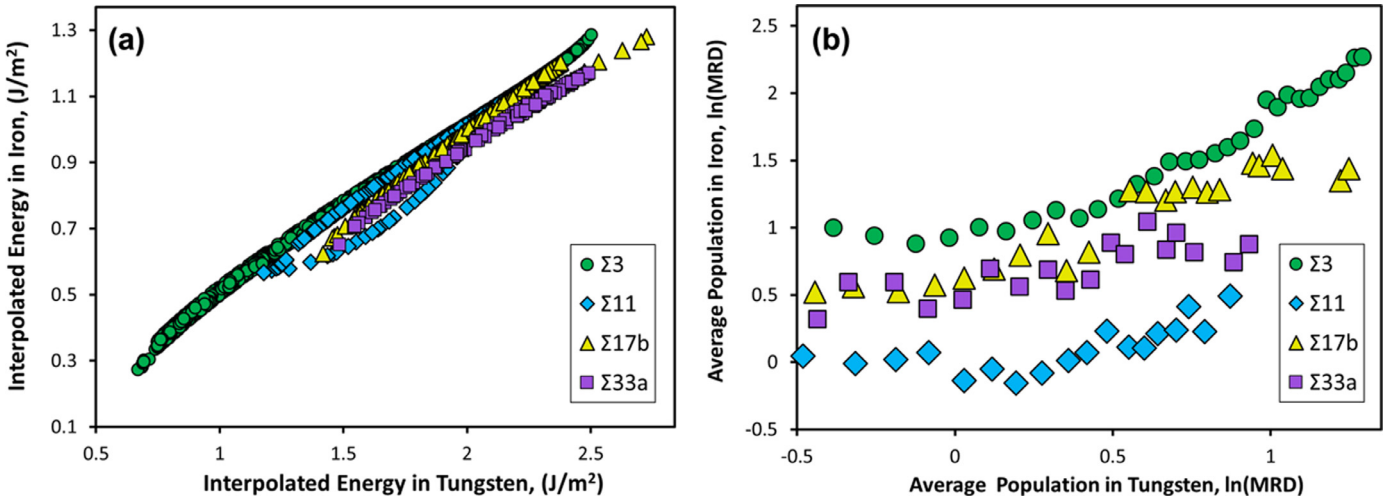

Fig. 4. The relationships between the interpolated energies (a) and the measured grain boundary populations (b) for the high-energy anisotropy boundaries in tungsten and iron: Σ3 (green circles), Σ11 (blue diamonds), Σ17b (yellow triangles), and Σ33a (purple squares). For comparisons of the average populations in (b), all grain boundaries at each misorientation in tungsten are discretized with an interval of 0.1 MRD and the average populations of the isostructural boundaries in iron are plotted using a logarithmic scale. Note that the interpolated energies in tungsten and iron are derived respectively from the functions proposed in this study and in [11]. The grain boundary populations in the nanocrystalline tungsten and the ferritic steel (α-Fe) were measured by using a transmission electron microscope orientation mapping technique [20] and three-dimensional electron backscatter diffraction, respectively [10] (For interpretation of the references to color in this figure legend, the reader is referred to the web version of this article.).

minimum energies or energy cusps at each misorientation. For the high-energy anisotropy boundaries, the inverse relationships between the grain boundary population and energies for the Σ3 and Σ11 misorientations are consistent with previous studies of BCC materials [10,14], however the inverse relationships for the Σ17b and Σ33a had never been reported due to the limited scope of the energy data sets for these misorientations. It should be noted that the slopes of the inverse relationships for Σ3 (−0.74), Σ11 (−1.01), Σ17b (−1.17), and Σ33a (−1.01) misorientations are different from those determined for FCC metals [8,9,25].

Fig. 4 shows comparisons between grain boundary area and energy distributions for the four misorientations: Σ3, Σ11, Σ17b, and Σ33a in tungsten and ferritic steel (α-Fe). As shown in Fig. 4**a**, the interpolated grain boundary energies in tungsten are all linearly correlated with the energies of the same boundaries in iron interpolated from the energy function recently reported in [11], indicating that the isostructural boundary specified by the five macroscopic degrees of freedom governs the variation of grain boundary energies in the two BCC metals. While not shown here, the grain boundary population and energies for the high-energy anisotropy

misorientations (i.e. Σ3, Σ11, Σ17b, and Σ33a) in iron [11] are also inversely correlated, similar to what have been observed for tungsten in Fig. 3**b**. To quantify the similarity between the grain boundary populations at each misorientation, all grain boundaries in tungsten are first sorted into intervals of 0.1 MRD, and then the average populations of isostructural boundaries in the two metals are calculated for each interval and plotted using a logarithmic scale in Fig. 4**b**. It is found that the relative populations as well as the slopes of the linear correlations at each misorientation in the two metals are different. Consequently, the GBCDs in the two BCC metals are not only governed by the grain boundary energies but strongly influenced by other parameters associated with the materials processing routes, consistent with the previous studies for FCC metals (copper and aluminum) [9,18].

The one-dimensional disorientation angle distribution, even though it integrates over the variations of population with disorientation axis and grain boundary plane orientation, frequently shows maxima associated with high population boundaries [26,27]. BCC metals have been shown to display a wide variety of disorientation angle distributions (including random, unimodal, and bimodal distributions) that can be specifically controlled using thermomechanical processes [20,27–30]. The fact that it is able to control the relative populations of specific grain boundary types (misorientations) suggests that it is possible to GBE BCC metals. The populations of the coherent twin boundary in BCC metals (Σ3/{211}) are much lower than in FCC metals (Σ3/{111}) [8–10,14–16], except for the case of ferritic steel (40 MRD) [17] and well-annealed polycrystalline aluminum (28 MRD) [31]. During grain growth and microstructure evolution, the energy needed to form a coherent twin in an FCC metal is less than in a BCC metal, and as a result, higher fractions of the coherent twin boundaries are usually observed in the FCC metals [8–10,14–18]. Interestingly, a significant enhancement of the populations of the coherent twin boundary in the aluminum thin film prepared by sputter deposition (700 MRD) suggests that the columnar structure with a strong ⟨111⟩ fiber texture could play a major role for the GBE films [18]. It should be noted that the population of the coherent twin boundary in the tungsten thin film (2.9 MRD) is much lower than the ones in the aluminum thin film although these two specimens are both prepared by using the sputter deposition technique [18,20]. The sputter-deposited tungsten thin film is not a single phase as in the case of the aluminum and the tungsten thin film is annealed at 850 °C for 2 h in an Ar-H_2 atmosphere to transform the remaining metastable beta tungsten (A15) to the BCC. The phase transformation in the annealed tungsten thin film reduces the crystallographic texture and this leads to the random disorientation angle distribution (Fig. 2**a**) [20]. Therefore, extensive investigations of recovery, recrystallization, and grain growth that influences the disorientation angle distribution or the GBCD would be needed prior to employing GBE for BCC metals. The grain boundary energy function for tungsten proposed in this study would benefit simulations of the GBCD evolution and promote the application of GBE to tungsten.

In summary, the grain boundary energy anisotropy in tungsten is accurately described by a grain boundary energy function developed by fitting values from atomistic simulations to the RSW function. Based on the extensive grain boundary energy data sets derived from the energy function, it is clearly demonstrated that the inverse relationships between the relative areas and energies in tungsten are only observed for high-energy anisotropy boundaries (i.e. Σ3, Σ11, Σ17b, and Σ33a). A Matlab® script, WGBE.m, which was used to compute the energy function is available in supplementary data.

This work was supported by the Research Strengthening Project of the Faculty of Engineering, King Mongkut's University of Technology Thonburi (KMUTT). O.C. acknowledges financial support from the Faculty of Science, KMUTT, and the Thailand Institute of Nuclear Technology (TINT). S.R. acknowledges the supports provided by the Thailand Science Research and Innovation(TSRI) under Fundamental Fund (Project: Advanced Materials and Manufacturing for Applications in New S-curve Industries), the Development and Promotion of Science and Technology Talents Project (DPST) and thanks Prof. Worawat Meevasana for invaluable discussions and suggestions. T.O. and T.F. acknowledges support from the Lawrence Livermore National Lab. LDRD program. Lawrence Livermore National Laboratory is operated by Lawrence Livermore National Security, LLC, for the U.S. Department of Energy, National Nuclear Security Administration under Contract DE-AC52–07NA27344.

Declaration of Competing Interest

The authors declare that they have no known competing financial interests or personal relationships that could have appeared to influence the work reported in this paper.

Supplementary materials

Supplementary material associated with this article can be found, in the online version, at doi:10.1016/j.scriptamat.2021.114384.

References

[1] H. Van Swygenhoven, J.R. Weertman, Materials Today 9 (2006) 24–31, doi:10.1016/S1369-7021(06)71494-8).
[2] T. Watanabe, J Mater Sci 46 (2011) 4095–4115, doi:10.1007/s10853-011-5393-z).
[3] V. Randle, Materials Science and Technology 26 (2010) 253–261, doi:10.1179/026708309X12601952777747.
[4] J. Roth, E. Tsitrone, A. Loarte, Th. Loarer, G. Counsell, R. Neu, V. Philipps, S. Brezinsek, M. Lehnen, P. Coad, Ch. Grisolia, K. Schmid, K. Krieger, A. Kallenbach, B. Lipschultz, R. Doerner, R. Causey, V. Alimov, W. Shu, O. Ogorodnikova, A. Kirschner, G. Federici, A. Kukushkin, Journal of Nuclear Materials 390–391 (2009) 1–9, doi:10.1016/j.jnucmat.2009.01.037.
[5] M.R. Gilbert, S.L. Dudarev, S. Zheng, L.W. Packer, J.-C. Sublet, Nucl. Fusion 52 (2012) 083019, doi:10.1088/0029-5515/52/8/083019.
[6] Y. Cheng, M. Mrovec, P. Gumbsch, Philosophical Magazine 88 (2008) 547–560, doi:10.1080/14786430801894577.
[7] Z. Yang, L. Hu, D. Maroudas, K.D. Hammond, Journal of Applied Physics 123 (2018) 225104, doi:10.1063/1.5026617).
[8] S. Ratanaphan, R. Sarochawikasit, N. Kumanuvong, S. Hayakawa, H. Beladi, G.S. Rohrer, T. Okita, J Mater Sci 54 (2019) 5570–5583, doi:10.1007/s10853-018-03297-4).
[9] S. Ratanaphan, D. Raabe, R. Sarochawikasit, D.L. Olmsted, G.S. Rohrer, K.N. Tu, J Mater Sci 52 (2017) 4070–4085, doi:10.1007/s10853-016-0670-5).
[10] H. Beladi, G.S. Rohrer, Acta Materialia 61 (2013) 1404–1412, doi:10.1016/j.actamat.2012.11.017.
[11] R. Sarochawikasit, C. Wang, P. Kumam, H. Beladi, T. Okita, G.S. Rohrer, S. Ratanaphan, Materialia 19 (2021) 101186, doi:10.1016/j.mtla.2021.101186.
[12] E.A. Holm, D.L. Olmsted, S.M. Foiles, Scripta Materialia 63 (2010) 905–908, doi:10.1016/j.scriptamat.2010.06.040.
[13] S. Ratanaphan, D.L. Olmsted, V.V. Bulatov, E.A. Holm, A.D. Rollett, G.S. Rohrer, Acta Materialia 88 (2015) 346–354, doi:10.1016/j.actamat.2015.01.069.
[14] S. Ratanaphan, T. Boonkird, R. Sarochawikasit, H. Beladi, K. Barmak, G.S. Rohrer, Materials Letters 186 (2017) 116–118, doi:10.1016/j.matlet.2016.09.104.
[15] G.S. Rohrer, J. Li, S. Lee, A.D. Rollett, M. Groeber, M.D. Uchic, Materials Science and Technology 26 (2010) 661–669, doi:10.1179/026708309X12468927349370.
[16] S. Ratanaphan, Grain Boundary Character Distributions in Isostructural Materials, Carnegie Mellon University, 2013.
[17] H. Beladi, G.S. Rohrer, Metall Mater Trans A 48 (2017) 2781–2790, doi:10.1007/s11661-016-3630-4).
[18] G.S. Rohrer, X. Liu, J. Liu, A. Darbal, M.N. Kelly, X. Chen, M.A. Berkson, N.T. Nuhfer, K.R. Coffey, K. Barmak, J Mater Sci 52 (2017) 9819–9833, doi:10.1007/s10853-017-1112-8).
[19] X. Fang, K. Zhang, H. Guo, W. Wang, B. Zhou, Materials Science and Engineering: A 487 (2008) 7–13, doi:10.1016/j.msea.2007.09.075.
[20] X. Liu, D. Choi, H. Beladi, N.T. Nuhfer, G.S. Rohrer, K. Barmak, Scripta Materialia 69 (2013) 413–416, doi:10.1016/j.scriptamat.2013.05.046.
[21] V.V. Bulatov, B.W. Reed, M. Kumar, Acta Materialia 65 (2014) 161–175, doi:10.1016/j.actamat.2013.10.057.
[22] D. Wolf, Scripta Metallurgica 23 (1989) 1713–1718, doi:10.1016/0036-9748(89)90348-7).
[23] H. Dette, J. Gösmann, C. Greiff, R. Janisch, Acta Materialia 125 (2017) 145–155, doi:10.1016/j.actamat.2016.11.044.

[24] A. Morawiec, K. Glowinski, Acta Materialia 61 (2013) 5756–5767, doi:10.1016/j.actamat.2013.06.019.
[25] E.A. Holm, G.S. Rohrer, S.M. Foiles, A.D. Rollett, H.M. Miller, D.L. Olmsted, Acta Materialia 59 (2011) 5250–5256, doi:10.1016/j.actamat.2011.05.001.
[26] H. Beladi, P. Cizek, P.D. Hodgson, Metall Mater Trans A 40 (2009) 1175–1189, doi:10.1007/s11661-009-9799-z).
[27] H. Beladi, G.S. Rohrer, Metall Mater Trans A 44 (2013) 115–124, doi:10.1007/s11661-012-1393-0).
[28] W. Wang, Y. Cui, G.S. Rohrer, C. Cai, S. Chen, X. Gu, Y. Lin, Scripta Materialia 170 (2019) 62–66, doi:10.1016/j.scriptamat.2019.05.033.
[29] S. Kobayashi, W. Yang, Y. Tomobe, R. Okada, S. Tsurekawa, J Mater Sci 55 (2020) 9273–9285, doi:10.1007/s10853-020-04555-0).
[30] S. Kobayashi, S. Tsurekawa, T. Watanabe, A. Kobylanski, Philosophical Magazine 88 (2008) 489–506, doi:10.1080/14786430801891748.
[31] D.M. Saylor, B.S. El Dasher, A.D. Rollett, G.S. Rohrer, Acta Materialia 52 (2004) 3649–3655, doi:10.1016/j.actamat.2004.04.018.